23. B. D. Tapley, S. Bettadpur, J. C. Ries, P. F. Thompson, M. M. Watkins, *Science* **305**, 503–505 (2004).
24. I. Velicogna, J. Wahr, *Science* **311**, 1754–1756 (2006).
25. S. B. Luthcke, A. A. Arendt, D. D. Rowlands, J. J. McCarthy, C. F. Larsen, *J. Glaciol.* **54**, 767–777 (2008).
26. A. S. Gardner *et al.*, *Nature* **473**, 357–360 (2011).
27. T. Jacob, J. Wahr, W. T. Pfeffer, S. Swenson, *Nature* **482**, 514–518 (2012).
28. G.-Y. Niu *et al.*, *Geophys. Res. Lett.* **34**, L15704 (2009).
29. M. Rodell, I. Velicogna, J. S. Famiglietti, *Nature* **460**, 999–1002 (2009).
30. J. S. Famiglietti *et al.*, *Geophys. Res. Lett.* **38**, L03403 (2011).
31. H. Kim, P. J.-F. Yeh, T. Oki, S. Kanae, *Geophys. Res. Lett.* **36**, L17402 (2009).
32. G. Ramillien *et al.*, *Global Planet. Change* **60**, 381–392 (2008).
33. P. C. D. Milly *et al.*, in *Understanding Sea-Level Rise and Variability*, J. A. Church, P. L. Woodworth, T. Aarup, W. S. Wilson, Eds. (Wiley-Blackwell, 2010), pp. 226–255.
34. W. Llovel, M. Becker, A. Cazenave, J.-F. Crétaux, G. Ramillien, *C. R. Geosci.* **342**, 179–188 (2010).
35. R. Rietbroek, S.-E. Brunnabend, J. Kusche, J. Schroeter, C. Dahle, *Proc. Natl. Acad. Sci. U.S.A.* 10.1073/pnas.1519132113 (2015).
36. M. M. Watkins, D. N. Wiese, D.-N. Yuan, C. Boening, F. W. Landerer, *J. Geophys. Res. Solid Earth* **120**, 2648–2671 (2015).
37. W. R. Peltier, D. F. Argus, R. Drummond, *J. Geophys. Res. Solid Earth* **120**, 450–487 (2015).
38. M. Cheng, B. D. Tapley, *J. Geophys. Res.* **109** (B9), B09402 (2004).
39. J. Wahr, R. S. Nerem, S. V. Bettadpur, *J. Geophys. Res. Solid Earth* **120**, 4597–4615 (2015).
40. S. Swenson, D. Chambers, J. Wahr, *J. Geophys. Res.* **113** (B8), B08410 (2008).
41. S.-C. Han, R. Riva, J. Sauber, E. Okal, *J. Geophys. Res. Solid Earth* **118**, 1240–1267 (2013).
42. R. Riva, J. Bamber, D. Lavallee, B. Wouters, *Geophys. Res. Lett.* **37**, L19605 (2010).
43. W. Llovel, J. K. Willis, F. W. Landerer, I. Fukumori, *Nature Climate Change* **4**, 1031–1035 (2014).
44. Materials and methods are available as supplementary materials on *Science* Online.
45. J. T. Reager, B. F. Thomas, J. S. Famiglietti, *Nat. Geosci.* **7**, 588–592 (2014).
46. J. L. Chen, C. R. Wilson, B. D. Tapley, *Water Resour. Res.* **46**, W12526 (2010).
47. G. Ramillien, F. Frappart, L. Seoane, *Remote Sens.* **6**, 7379–7405 (2014).
48. E. Forootan *et al.*, *Surv. Geophys.* **35**, 913–940 (2014).
49. J. T. Reager, J. S. Famiglietti, *Geophys. Res. Lett.* **36**, L23402 (2009).
50. J. T. Fasullo, C. Boening, F. W. Landerer, R. S. Nerem, *Geophys. Res. Lett.* **40**, 4368–4373 (2013).
51. K. A. Voss *et al.*, *Water Resour. Res.* **49**, 904–914 (2013).
52. E. Forootan *et al.*, *Remote Sens. Environ.* **140**, 580–595 (2014).
53. B. R. Scanlon, L. Longuevergne, D. Long, *Water Resour. Res.* **48**, W04520 (2012).
54. B. R. Scanlon *et al.*, *Proc. Natl. Acad. Sci. U.S.A.* **109**, 9320–9325 (2012).
55. W. Feng *et al.*, *Water Resour. Res.* **49**, 2110–2118 (2013).



### ACKNOWLEDGMENTS

We thank M. Watkins, E. Ivins, D. Argus, G. Cogley, A. Richey, Y. Wada, R. Nerem, and D. Chambers for their contributions and discussion. This work was supported by funding from the NASA NEWS, Sea Level, and Cryosphere programs; the NASA GRACE Science Team; and the University of California Multicampus Research Programs and Initiatives. This multidisciplinary collaboration grew from the interactions of the NASA Sea Level Change Team. The research was conducted at the University of California, Irvine and at the Jet Propulsion Laboratory, California Institute of Technology under contract with NASA. M.-H. Lo was supported by the Ministry of Science and Technology (MOST), Taiwan, MOST 103-2111-M-002-006. GRACE RL05M data are available at podaac.jpl.nasa.gov. The authors declare no competing interests.


### SUPPLEMENTARY MATERIALS

www.sciencemag.org/content/351/6274/699/suppl/DC1
Materials and Methods
Figs. S1 to S11
Tables S1 to S4
References (*56*–*69*)

9 November 2015; accepted 7 January 2016
10.1126/science.aad8386

MICROBIAL PHYSIOLOGY

# Artificial electron acceptors decouple archaeal methane oxidation from sulfate reduction

**Silvan Scheller,* Hang Yu, Grayson L. Chadwick, Shawn E. McGlynn,† Victoria J. Orphan***

**The oxidation of methane with sulfate is an important microbial metabolism in the global carbon cycle. In marine methane seeps, this process is mediated by consortia of anaerobic methanotrophic archaea (ANME) that live in syntrophy with sulfate-reducing bacteria (SRB). The underlying interdependencies within this uncultured symbiotic partnership are poorly understood. We used a combination of rate measurements and single-cell stable isotope probing to demonstrate that ANME in deep-sea sediments can be catabolically and anabolically decoupled from their syntrophic SRB partners using soluble artificial oxidants. The ANME still sustain high rates of methane oxidation in the absence of sulfate as the terminal oxidant, lending support to the hypothesis that interspecies extracellular electron transfer is the syntrophic mechanism for the anaerobic oxidation of methane.**

Biological methane oxidation in the absence of oxygen is restricted to anaerobic methanotrophic archaea (ANME) that are phylogenetically related to methanogens (*1*, *2*). These organisms evolved to metabolize methane to $CO_2$ near thermodynamic equilibrium ($E^{o\prime}$ = −245 mV for $CH_4/CO_2$) via the pathway of reverse methanogenesis (*3*), which includes the chemically challenging step of methane activation without oxygen-derived radicals (*4*). Reported terminal electron acceptors for anaerobic oxidation of methane (AOM) include sulfate (*1*, *2*), nitrate (*5*), and metal oxides (*6*). Nitrate reduction coupled to methane oxidation is directly mediated by a freshwater archaeal methanotroph "*Ca. Methanoperedens nitroreducens*" ANME-2d (*5*); however, the electron transport mechanism coupling methane oxidation with other terminal electron acceptors (such as sulfate and metal oxides) is still debated (*7*–*9*).

Sulfate-coupled methane oxidation (Eq. 1) is the dominant mechanism for methane removal within marine sediments, preventing the release of teragrams per year of this greenhouse gas from the oceans (*10*).

$$CH_4 + SO_4^{2-} = HCO_3^- + HS^- + H_2O$$
$$\text{Gibbs free energy } (\Delta G^{o\prime}) = -17 \text{ kJ mol}^{-1} \quad (1)$$

Multiple methanotrophic archaeal lineages (ANME-1; ANME-2a,b,c; and ANME-3) form syntrophic consortia with sulfate-reducing deltaproteobacteria (SRB) that drive AOM in areas of methane release at the seabed (*11*). The metabolism of AOM with sulfate appears to be partitioned between the two partners, requiring the exchange of electrons or intermediates. The mechanism underlying this syntrophic association has been studied using microcosm experiments [with AOM microorganisms exhibiting doubling times of 2 to 7 months (*12*–*17*)], as well as through the application of stable isotope analyses (*2*), radiotracer rate measurements (*18*), metagenomics (*3*, *5*, *19*, *20*), and theoretical modeling (*21*, *22*).

Attempts to metabolically decouple the syntrophic association and identify the intermediate compound passaged between ANME archaea and their SRB partners have been unsuccessful when diffusive intermediates such as hydrogen, acetate, formate, and some redox active organic electron shuttles were used (*16*, *23*). Culture-independent evidence for direct interspecies electron transfer in sulfate-coupled AOM by members of the ANME and their SRB partners (*8*, *9*) supports earlier genomic predictions of this process occurring in the methanotrophic ANME-1 (*19*).

Guided by the recent evidence of direct interspecies electron transfer from ANME-2 to SRB (*8*), we probed whether artificial electron acceptors can substitute for the role of the SRB partner as a terminal oxidant for AOM. Respiration of the artificial electron acceptor 9,10-anthraquinone-2,6-disulfonate (AQDS, $E^{o\prime}$ = −186 mV) has been previously reported in methanogens (*24*). We tested AQDS as a sink for methane-derived electrons generated by the ANME archaea in incubations with deep-sea methane seep sediment. The stoichiometry of methane oxidation coupled to AQDS predicts the reduction of four equivalents of AQDS per methane (Eq. 2).

$$CH_4 + 4\,AQDS + 3H_2O = HCO_3^- + H^+ + 4\,AQH_2DS$$
$$\Delta G^{o\prime} = -41 \text{ kJ mol}^{-1} \quad (2)$$

To quantify AOM with AQDS, we performed anaerobic microcosm experiments using methane seep sediment from the Santa Monica basin

Division of Geological and Planetary Sciences, California Institute of Technology, Pasadena, CA 91125, USA.
***Corresponding author. E-mail: vorphan@gps.caltech.edu (V.J.O.); scheller@caltech.edu (S.S.)** †Present address: Department of Biological Sciences, Tokyo Metropolitan University, Tokyo 192-0397, Japan; and Biofunctional Catalyst Research Team, RIKEN Center for Sustainable Resource Science, Saitama 351-0198, Japan.

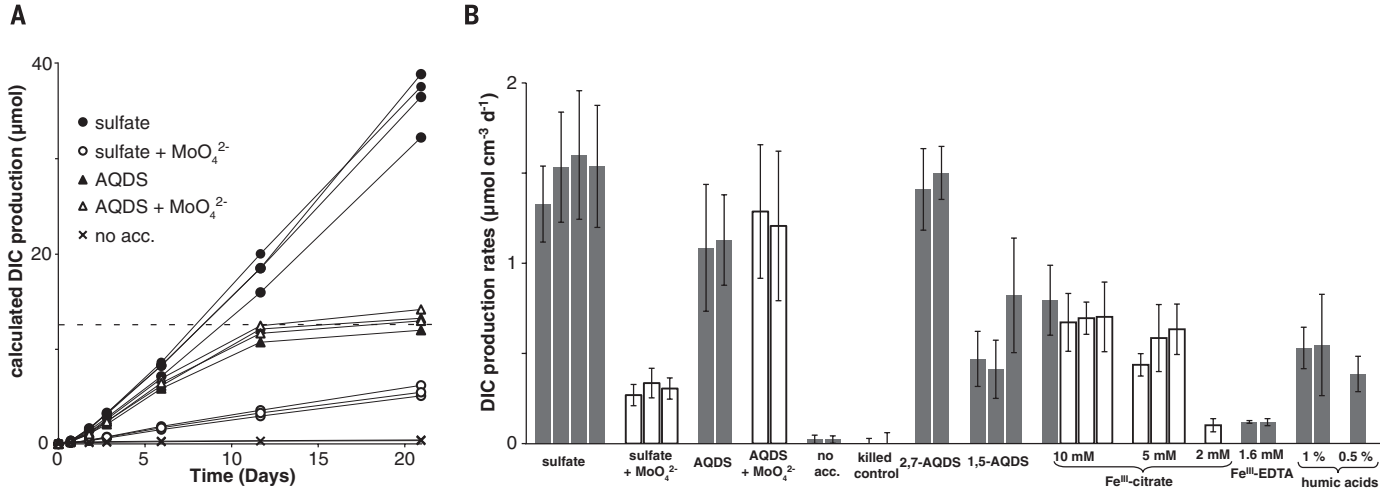


**Fig. 1. DIC production per vial in incubations with 1.0 cm$^3$ of methane seep sediment.** (**A**) Methane oxidation coupled to sulfate reduction [140 µmol of $SO_4^{2-}$ (28 mM), methane oxidation unlimited, circles], and methane oxidation coupled to AQDS reduction [50 µmol of AQDS (10 mM) in the absence of sulfate, triangles]. Due to the 1:4 stoichiometry between $CH_4$ and AQDS, the produced DIC plateaued at approximately 12.5 µmol (dashed line). Open symbols depict incubations with the addition of the sulfate-reduction inhibitor sodium molybdate (25 mM). Control incubations without electron acceptors added (x symbol). (**B**) Initial rates of methane oxidation with different electron acceptors for individual incubation bottles. Values from the linear regression of time points 1 to 6 days (four points) are calculated per cubic centimeter of wet sediment; error bars represent the 95% confidence interval. White bars depict incubations with sodium molybdate (25 mM). Time course measurements for these experiments are provided in fig. S1; raw data are provided in fig. S2.

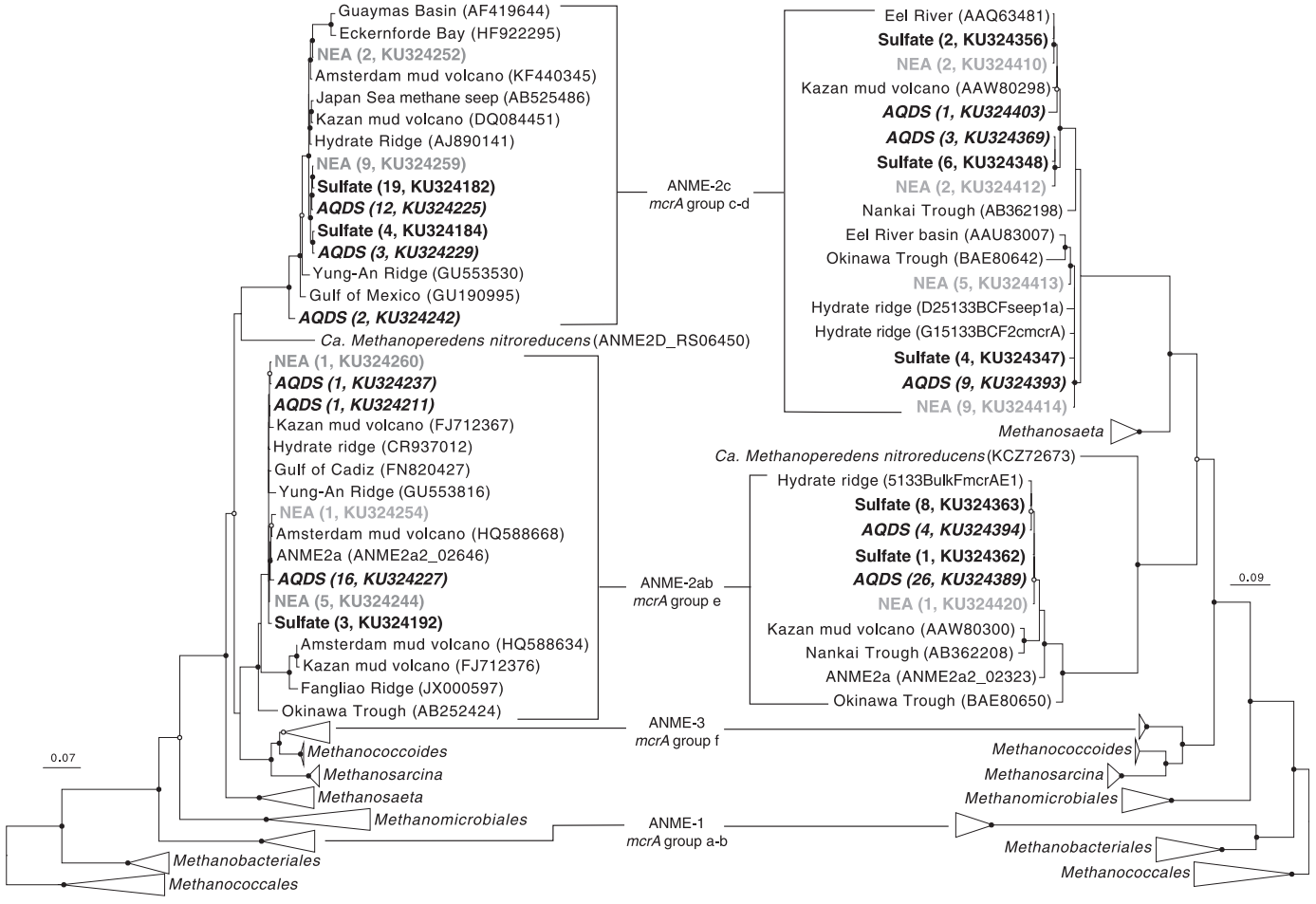


**Fig. 2. Bayesian phylogeny of expressed archaeal RNA recovered from different AOM microcosms.** 16S rRNA (left) and mcrA (right) transcripts obtained from AOM incubations with either sulfate or AQDS as the primary oxidant (bold text) or no electron acceptor added (NEA, gray text). Numbers in parentheses represent numbers of sequences recovered for each taxa. Bayesian likelihood values >75 and >90% are indicated by open and solid circles, respectively. Scale bars represent estimated sequence divergence or amino acid changes.

that had been rendered sulfate- and sulfide-free (*25*) and amended with 50 μmol AQDS and $^{13}$C-labeled methane [0.35 MPa (*25*)]. After a 21-day incubation at 4°C, approximately 12.5 μmol of dissolved inorganic carbon (DIC) formed from the $^{13}$C-methane (Fig. 1A), concomitant with the reduction of AQDS close to the predicted 1:4 stoichiometry (table S1). The initial rates of AOM with AQDS were equivalent to the rates measured with sulfate over the first 6 days (Fig. 1B) and later diverged as the AQDS was depleted from solution. At 22.5°C, where AQDS has higher solubility (table S2), the AOM rates with AQDS exceeded those with sulfate (fig. S3).

To confirm that the observed methane oxidation with AQDS was not coupled to traces of sulfate, we tracked AOM in the presence of sodium molybdate, a competitive inhibitor for sulfate reduction (*26*). With the addition of 25 mM molybdate, rates of sulfate-coupled AOM decreased by approximately fivefold relative to controls, which is consistent with previous reports (*16*). The high rates of methane oxidation in our sulfate-free incubations containing AQDS showed no inhibitory response if molybdate was included, indicating a decoupling of AOM from sulfate-reduction (Fig. 1, A and B).

Stimulation of AOM without sulfate is not restricted to AQDS. Regioisomers of AQDS (1,5-AQDS and 2,7-AQDS), humic acids, and soluble iron(III) complexes (ferric citrate and ferric-EDTA) also stimulated anaerobic oxidation of methane at rates that were at least 0.1 μmol cm$^{-3}$ day$^{-1}$ (Fig. 1B; a list of all oxidants tested is provided in table S3). In control incubations without an added electron acceptor, we measured a small apparent methane oxidation activity (1.5% relative to sulfate-coupled AOM, Fig. 1B) that is probably attributed to enzyme-catalyzed isotope exchange between methane and DIC without net methane oxidation (*27*, *28*). In killed control experiments (formaldehyde addition), we did not detect any conversion of $^{13}$C-methane to DIC (Fig. 1B).

The archaeal 16*S* ribosomal RNA (rRNA) gene diversity of the seep sediment used in our AOM microcosm experiments was dominated by ANME-2 of the subgroups ANME-2a and ANME-2c, with a low relative abundance of ANME-1 phylotypes (fig. S4). To identify the active archaea potentially involved in methane oxidation in our experiments, after 4 weeks, we sequenced expressed archaeal 16*S* rRNA and the alpha subunit of the methyl coenzyme M reductase (mcrA) from microcosm treatments containing either sulfate, AQDS, or no added electron acceptor. The archaeal sequences recovered from the 16*S* rRNA and mcrA cDNA clone libraries were similar in the three treatments, with each containing only representatives of ANME-2a and -2c (Fig. 2). The detection of transcripts from multiple subgroups of ANME-2 in each treatment suggests that the same ANME lineages are active in AOM, independent of whether sulfate or AQDS is supplied as the oxidant. In contrast to the similar ANME composition, the relative abundance of recovered bacterial SRB clones (e.g. Desulfobacteraceae SEEP-SRB1) in the cDNA libraries decreased in treatments lacking sulfate as compared to microcosms supporting active sulfate-coupled AOM (table S4), and suggests that ANME may be capable of using AQDS directly without syntrophic interaction.

To directly test this hypothesis, we used cell-specific stable isotope analysis to quantify the anabolic activity of ANME-2 (including ANME-2c) and their co-associated syntrophic partners in consortia recovered from incubations supplied with different oxidants (including sulfate, AQDS, humic acids, and ferric iron). Using $^{15}NH_4^+$ stable isotope probing combined with fluorescence in situ hybridization and nanoscale secondary ion mass spectrometry [FISH-SIMS (*2*)], we measured the cell-specific anabolic activity ($^{15}$N cellular enrichment) in paired ANME and SRB populations in consortia (*8*). After 18 days of incubation with $^{15}NH_4^+$, consortia were phylogenetically identified by FISH using ANME-2c and Desulfobacteraceae-targeted oligonucleotide probes and were analyzed by nanoSIMS to quantify the assimilation of $^{15}NH_4^+$ for each paired population of ANME-2 and SRB (*25*).

In AOM microcosms containing sulfate, the $^{15}NH_4^+$ assimilation by co-associated bacteria and archaea in consortia from two sets of experiments ($n$ = 20 and $n$ = 19 consortia) was positively correlated at a ratio of approximately 1:1, indicating balanced syntrophic growth during AOM similar to (*8*) (Fig. 3C and Fig. 4, A and B). ANME-SRB consortia recovered from sulfate-free incubations amended with AQDS also showed high levels of $^{15}NH_4^+$ assimilation; however, in this case, anabolic activity within each of these consortia occurred only in the ANME archaea and not in their co-associated bacterial partners (Figs. 3F and 4A). This is consistent with the weak FISH signal observed for the Desulfobacteraceae. These data offer direct validation of results based on RNA analysis, demonstrating that when AQDS was supplied as the terminal electron acceptor for AOM, the ANME-2 archaea sustained active biosynthesis that was decoupled from the activity of the SRB partner. This was directly shown for ANME-2c ($n$ = 11 consortia) and inferred for ANME-2a on the basis of nanoSIMS results from the eight non–ANME-2c aggregates that were all anabolically active. Consortia from incubations with methane and $^{15}NH_4^+$, but lacking an electron acceptor, showed no measurable anabolic activity in either partner ($n$ = 9 ANME-SRB consortia; Fig. 4A, inset, and fig. S5).

The ANME cells paired with SRB in consortia from AQDS incubations showed similar levels of anabolic activity [3.3 months doubling time based on average $^{15}$N incorporation (*25*)] as those of ANME archaea conserving energy through conventional sulfate-coupled AOM [2.9 months doubling time (*25*)] in parallel incubations, suggesting equivalent potential for growth (Fig. 4A).

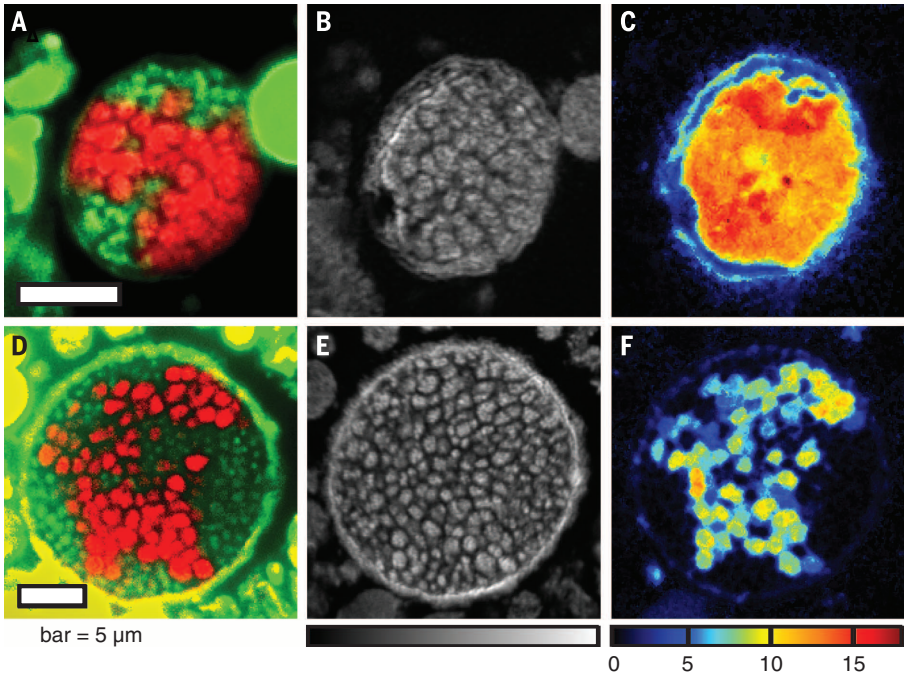


**Fig. 3. Representative FISH-nanoSIMS images from sulfate and AQDS microcosms.** The correlation between phylogenetic identity (FISH) and anabolic activity ($^{15}$N enrichment) for example consortia of ANME-2c archaea and sulfate-reducing bacteria analyzed from AOM incubations amended with sulfate or AQDS is shown. (**A** to **C**) AOM consortium from microcosm with sulfate. (**D** to **F**) Consortium from microcosm with AQDS as the sole electron acceptor. In each case, the at % of $^{15}$N isotope enrichment was calculated from ratios of secondary ion images of $^{12}C^{15}N^-$ and $^{12}C^{14}N^-$. (A) and (D) FISH images, with ANME-2c in red and Desulfobacteraceae in green; the FISH signal for the bacterial cells in (D) is weak, probably due to the low abundance of cellular rRNA in SRB in the AQDS treatment without sulfate. (B) and (E) nanoSIMS ion image of $^{12}C^{14}N^-$ for cellular biomass, linear scale (0 to 4500 counts per pixel). (C) and (F) Fractional abundance of $^{15}$N (in at %) as a proxy for anabolic activity.

Apparently, ANME-2 archaea are capable of conserving energy for biosynthesis independent of sulfate availability and separated from the activity of their syntrophic bacterial partners.

AOM incubations with iron(III)-citrate and humic acids as the alternative electron acceptors also demonstrated exclusive biosynthetic activity of ANME-2c and other ANME-2 cells (Fig. 4B and fig. S6). In contrast to incubations with sulfate or AQDS, only a few and mostly small AOM consortia [14 out of 31 for iron(III)-citrate and 4 out of 46 for humic acids] were anabolically active (>10% archaeal activity relative to cells in the sulfate treatments, or >0.8 atomic % (at %) of $^{15}N$), despite the high rates of AOM measured with those compounds (Fig. 1B).

All compounds that were able to replace the role of the SRB partners during AOM, including AQDS isomers, humic acids, and iron(III) complexes, have the ability to accept single electrons. Mechanistically, extracellular electron transfer (*8*, *9*) from ANME-2 to single electron acceptors can account for all our findings. Large, S-layer–associated multi-heme c-type cytochromes in members of the ANME-2 archaea (*8*) could putatively conduct electrons [discussed in (*29*)] derived from reverse methanogenesis from the archaeal membrane to the outside of the cell, where they can be taken up by a suitable electron acceptor. A congruent path of extracellular electron transfer has been proposed for the bacterium *Geobacter sulfurreducens* when oxidizing acetate coupled to the reduction of AQDS or humic acids (*30*). The similar catabolic and anabolic activities observed within ANME-2 archaea, independent of whether the terminal electron acceptor is AQDS or sulfate, suggest that the biochemistry within these organisms may follow the same pathway under AQDS conditions as when syntrophically coupled to SRB. Our data therefore also lend experimental evidence in support of the hypothesis of direct interspecies electron transfer as the syntrophic coupling mechanism between methane-oxidizing ANME-2 and SRB in the environment (*8*).

The apparent ability of ANME-2 to oxidize methane via the release of single electrons constitutes a versatile half-metabolism. This physiology suggests that methanotrophic ANME-2 archaea should also be able to respire solid electron acceptors directly via extracellular metal reduction, which would explain methane oxidation coupled to insoluble iron(III) and manganese(IV) reduction reported previously (*6*). Evolutionarily, methane oxidation with metal oxides could have served as a transient life style for ANME before the establishment of a syntrophic association with SRB. According to this hypothesis, methanogenic archaea first evolved the capability to conserve energy as a methanotroph coupled with the respiration of solid metal oxides as electron acceptors. In a subsequent evolutionary step, SRB developed a symbiosis with ANME archaea, gaining a direct source of electrons for sulfate reduction and leading to the highly structured syntrophic consortia common today in seep environments. This physiology of using extracellular electron transfer to enable syntrophic interaction (*8*, *9*) has the advantage that intermediates cannot be lost via diffusion and that electrical conductance is much faster than diffusive transfer of reducing equivalents (*8*). Further, this described metabolism may have industrial utility, providing a mechanism for the conversion of methane to $CO_2$ plus single electrons that can be catalyzed reversibly at low temperatures, with the potential to convert methane to electricity at high overall efficiencies. Finally, these findings offer a promising path forward for isolating members of the ANME-2 in pure culture, enabling detailed characterization of the ecophysiology of these key players in the global methane cycle.

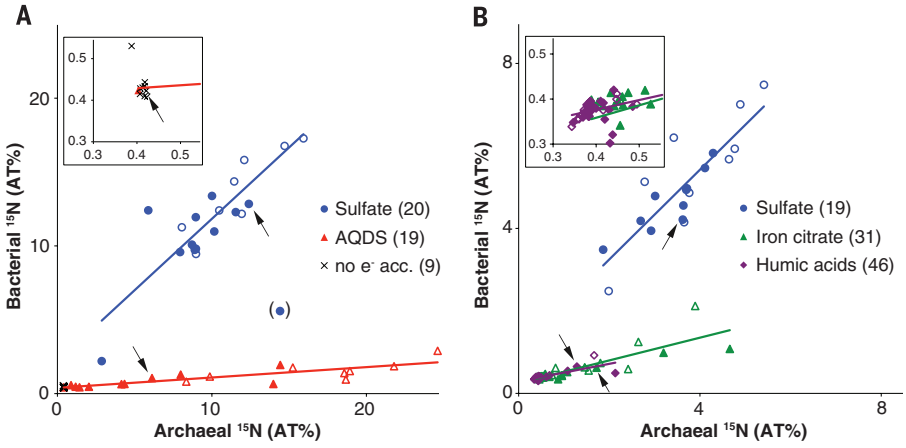


**Fig. 4. Summary of FISH-nanoSIMS $^{15}N$ incorporation data.** Average anabolic activity for paired ANME and SRB populations in each AOM consortium from incubations with different terminal electron experiments is shown. Each solid symbol represents the average $^{15}N$ at % for the population of paired ANME-2c cells relative to bacterial cells in a single consortium. Open symbols represent other unidentified ANME-SRB consortia (putative ANME-2a). (Insets) $^{15}N$ at % values close to natural abundance value (0.36 at % $^{15}N$). FISH-nanoSIMS images of consortia marked with an arrow are displayed in Fig. 3 and figs. S5 and S6. (A) and (B) constitute two independent sets of experiments; experiments in (A) contained ~80% $^{15}NH_4^+$, whereas those in (B) contained ~40% (*25*). Numeric data for each aggregate are provided in table S5. The activity of bacterial cells (b) relative to the archaeal cell activity (a) was determined via linear regression as follows: (**A**) Sulfate: b = 0.97a + 2.17, $R^2$ = 0.75; AQDS: b = 0.070a + 0.39, $R^2$ = 0.69. (**B**) Sulfate: b = 1.09a + 1.07, $R^2$ = 0.74; iron citrate: b = 0.28a + 0.25, $R^2$ = 0.71; humic acids: b = 0.21a + 0.29, $R^2$ = 0.60. The blue data point in parentheses (A) was not included for the linear regression (see fig. S7 for single-cell analysis and further discussion). The small apparent $^{15}N$ enrichment in bacteria from sulfate-free incubations was found to be due to inaccuracies in pixel assignments for SRB cells during data processing, determined by manual inspection of each nanoSIMS image.

## REFERENCES AND NOTES


1. A. Boetius *et al.*, *Nature* **407**, 623–626 (2000).
2. V. J. Orphan, C. H. House, K. U. Hinrichs, K. D. McKeegan, E. F. DeLong, *Science* **293**, 484–487 (2001).
3. S. J. Hallam *et al.*, *Science* **305**, 1457–1462 (2004).
4. S. Scheller, M. Goenrich, R. Boecher, R. K. Thauer, B. Jaun, *Nature* **465**, 606–608 (2010).
5. M. F. Haroon *et al.*, *Nature* **500**, 567–570 (2013).
6. E. J. Beal, C. H. House, V. J. Orphan, *Science* **325**, 184–187 (2009).
7. J. Milucka *et al.*, *Nature* **491**, 541–546 (2012).
8. S. E. McGlynn, G. L. Chadwick, C. P. Kempes, V. J. Orphan, *Nature* **526**, 531–535 (2015).
9. G. Wegener, V. Krukenberg, D. Riedel, H. E. Tegetmeyer, A. Boetius, *Nature* **526**, 587–590 (2015).
10. W. S. Reeburgh, *Chem. Rev.* **107**, 486–513 (2007).
11. K. Knittel, A. Boetius, *Annu. Rev. Microbiol.* **63**, 311–334 (2009).
12. P. R. Girguis, A. E. Cozen, E. F. DeLong, *Appl. Environ. Microbiol.* **71**, 3725–3733 (2005).
13. V. J. Orphan, K. A. Turk, A. M. Green, C. H. House, *Environ. Microbiol.* **11**, 1777–1791 (2009).
14. R. J. W. Meulepas *et al.*, *Biotechnol. Bioeng.* **104**, 458–470 (2009).
15. T. Holler *et al.*, *ISME J.* **5**, 1946–1956 (2011).
16. K. Nauhaus, T. Treude, A. Boetius, M. Krüger, *Environ. Microbiol.* **7**, 98–106 (2005).
17. K. Nauhaus, M. Albrecht, M. Elvert, A. Boetius, F. Widdel, *Environ. Microbiol.* **9**, 187–196 (2007).
18. S. B. Joye *et al.*, *Chem. Geol.* **205**, 219–238 (2004).
19. A. Meyerdierks *et al.*, *Environ. Microbiol.* **12**, 422–439 (2010).
20. F. P. Wang *et al.*, *ISME J.* **8**, 1069–1078 (2014).
21. M. J. Alperin, T. M. Hoehler, *Am. J. Sci.* **309**, 869–957 (2009).
22. B. Orcutt, C. Meile, *Biogeosciences* **5**, 1587–1599 (2008).
23. R. J. W. Meulepas, C. G. Jagersma, A. F. Khadem, A. J. M. Stams, P. N. L. Lens, *Appl. Microbiol. Biotechnol.* **87**, 1499–1506 (2010).
24. D. R. Bond, D. R. Lovley, *Environ. Microbiol.* **4**, 115–124 (2002).
25. Additional supplementary information is available on *Science* Online.
26. L. G. Wilson, R. S. Bandurski, *J. Biol. Chem.* **233**, 975–981 (1958).
27. T. Holler *et al.*, *Proc. Natl. Acad. Sci. U.S.A.* **108**, E1484–E1490 (2011).
28. M. Y. Yoshinaga *et al.*, *Nat. Geosci.* **7**, 190–194 (2014).
29. S. Pirbadian, M. Y. El-Naggar, *Phys. Chem. Chem. Phys.* **14**, 13802–13808 (2012).
30. J. W. Voordeckers, B. C. Kim, M. Izallalen, D. R. Lovley, *Appl. Environ. Microbiol.* **76**, 2371–2375 (2010).


## ACKNOWLEDGMENTS

We thank Y. Guan for assistance with the nanoSIMS, the Beckman Resource Center (BRCem) for sectioning, M. Aoki for FISH analysis of ANME-2a and ANME-2c consortia, and S. Goffredi and C. Skennerton for editorial comments. We are grateful to P. Brewer from the Monterey Bay Aquarium Research Institute

for providing the opportunity to participate in the 2013 research expedition and A. Pasulka and K. Dawson for their contributions in shipboard sample processing. This work was supported by the U.S. Department of Energy Biological and Environmental Research program (grants DE-SC0010574 and DE-SC0004940) and funding by the Gordon and Betty Moore Foundation through grants GBMF3306 and GBMF3780 (to V.J.O.). S.S. was supported in part by the Swiss National Science Foundation (grant no. PBEZP2_142903). All data are available in the supplementary materials. Archaeal 16S rRNA, mcrA genes, and bacterial 16S rRNA genes were deposited with the National Center for Biotechnology Information under accession numbers KU324182 to KU324260, KU324346 to KU324428, and KU324261 to KU324345, respectively. S.S., H.Y., and V.J.O. devised the study, and S.S., H.Y., G.L.C., and S.M. conducted the experiments and analyses. S.S. and V.J.O. wrote the manuscript, with contributions from all authors to data analysis, figure generation, and the final manuscript.

**SUPPLEMENTARY MATERIALS**

www.sciencemag.org/content/351/6274/703/suppl/DC1
Materials and Methods
Figs. S1 to S7
Tables S1 to S5
References (*31*–*57*)

26 October 2015; accepted 20 January 2016
10.1126/science.aad7154

LUNG PHYSIOLOGY

# Pulmonary neuroendocrine cells function as airway sensors to control lung immune response

**Kelsey Branchfield,[1] Leah Nantie,[1] Jamie M. Verheyden,[1] Pengfei Sui,[1] Mark D. Wienhold,[2] Xin Sun[1]***

**The lung is constantly exposed to environmental atmospheric cues. How it senses and responds to these cues is poorly defined. Here, we show that Roundabout receptor (*Robo*) genes are expressed in pulmonary neuroendocrine cells (PNECs), a rare, innervated epithelial population. *Robo* inactivation in mouse lung results in an inability of PNECs to cluster into sensory organoids and triggers increased neuropeptide production upon exposure to air. Excess neuropeptides lead to an increase in immune infiltrates, which in turn remodel the matrix and irreversibly simplify the alveoli. We demonstrate in vivo that PNECs act as precise airway sensors that elicit immune responses via neuropeptides. These findings suggest that the PNEC and neuropeptide abnormalities documented in a wide array of pulmonary diseases may profoundly affect symptoms and progression.**

In humans, approximately 5 to 8 liters of air passes in and out of the lung per minute when resting. The air can vary in oxygen and $CO_2$ concentration, may carry allergens, and confers different extents of mechanical stretch of the airway and gas-exchange surfaces. These signals are sensed, relayed, and processed into physiological outputs such as the control of pulmonary blood pressure, immune responses, and breathing rhythm, but the mechanism is unclear. Pulmonary neuroendocrine cells (PNECs) are found in a wide array of organisms from fish to mammals (*1*). In the mammalian lung, PNECs are the only innervated airway epithelial cells and represent less than 1% of the total lung epithelial cell population (*2*). Although in vitro evidence has implicated PNECs in oxygen sensing, bronchial and vascular smooth muscle tonus, and immune responses (*1*, *3*), these roles have not been demonstrated in vivo. A recent study showed that genetic ablation of PNECs in the adult did not compromise homeostasis or airway repair, leaving in question the in vivo importance of these cells (*4*). PNEC pathologies, in particular an increase in PNEC number, have been documented in a large array of lung diseases, including asthma, bronchopulmonary dysplasia, cystic fibrosis, chronic obstructive pulmonary disease, congenital diaphragmatic hernia, neuroendocrine hyperplasia of infancy, sudden infant death syndrome, and pulmonary hypertension (*5*–*8*). In each case, it remains unclear whether the PNEC increase is a cause for or the consequence of symptoms.

In mouse lung, most PNECs reside in clusters of ~3 to 20 cells called neuroepithelial bodies (NEBs) (*3*, *9*). Both solitary and clustered PNECs contain dense core vesicles, filled with bioactive neuropeptides such as calcitonin gene-related peptide (CGRP) or amines such as serotonin (*1*). These are released in response to stimuli, such as changes in oxygen level. Neuropeptides and amines have been implicated in some of the same processes as PNECs (*10*–*12*), raising the possibility that they may mediate PNEC function. However, a causal link has not been demonstrated in vivo.

We initiated the current study to uncover the mechanisms underlying congenital diaphragmatic hernia (CDH), a birth defect associated with considerable lung dysfunction, including heightened immune response and pulmonary hypertension (*13*). In a genetic mouse model of CDH, we uncovered a defect of failed PNEC clustering. This is followed by a sequence of events: an increase in PNEC neuropeptides, an increase in immune infiltrates, and remodeling of lung structure. These findings offer an in vivo demonstration of PNEC function. Because changes in PNEC number and associated neuropeptides have been documented in many lung diseases, our results have wide implications beyond CDH.

In humans, mutations in roundabout receptor (*ROBO*) genes have been associated with CDH (*13*, *14*). To study the lung defects associated with CDH, we inactivated both *Robo1* and *Robo2* in endoderm-derived epithelium, including the lung, using $Shh^{cre}$ (hereafter *Shhcre;Robo* mutant) in mice (*15*, *16*). Although these mutants survive, they exhibit reduced gas-exchange surface area starting at postnatal day (P) 15 (Fig. 1, A and B, and fig. S1). We performed microarray followed by quantitative reverse transcriptase polymerase chain reaction (qRT-PCR) at P7, before reduction of gas-exchange surface. Fifteen of the top 20 differentially expressed genes have been implicated in immune responses, and all are significantly increased, including *Ccl3*, *Cxcl2*, *Tnfa*, and *Saa3* (Fig. 1C). Consistent with this signature, we observed elevated numbers of immune cells, including neutrophils, eosinophils, macrophages, and T cells (Fig. 1, D and E, and fig. S2). Furthermore, there is an increase in the proportion of M2 and a decrease in the proportion of M1 macrophages (fig. S3). These findings indicate that *Shhcre;Robo* mutants show heightened immune sensitivity, mimicking a common CDH comorbidity (*13*).

Although *Robo* is expressed in the alveolar region of the lung mesenchyme (fig. S4), its expression in the epithelium is restricted to rare cells along the airway (Fig. 1F). Colabeling with CGRP antibody revealed that *Robo*-expressing epithelial cells are PNECs (Fig. 1G). To confirm that *Robo* genes are required within PNECs for function, we inactivated *Robo* using *Ascl1creERT2* (*17*), a knock-in cre driver that confers PNEC-specific activity in the lung epithelium (fig. S5). We found that *Ascl1creERT2;Robo* mutants exhibited both alveolar simplification and macrophage increase, recapitulating the *Shhcre;Robo* phenotypes (fig. S6). These findings together demonstrate that *Robo* is required specifically in PNECs for restricting immune cell number and preventing alveolar simplification.

At embryonic day (E) 13.5, newly specified PNECs were solitary cells in both control and *Shhcre;Robo* mutant lungs (Fig. 2, A and B). By E15.5, a majority of PNECs had aggregated into NEBs in the control. However, PNECs were not clustered in *Shhcre;Robo* mutants (Fig. 2, C and D). This highly penetrant phenotype persisted in postnatal lungs (Fig. 2, E and F, and fig. S7). Total PNEC cell number appears unaffected, as supported by normal expression of *Ascl1* and other PNEC markers (fig. S8). Unclustered cells

[1]Laboratory of Genetics, Department of Medical Genetics, University of Wisconsin-Madison, Madison, WI 53706, USA. [2]Department of Pediatrics, School of Medicine and Public Health, University of Wisconsin-Madison, Madison, WI 53706, USA.
*Corresponding author. E-mail: xsun@wisc.edu

# Artificial electron acceptors decouple archaeal methane oxidation from sulfate reduction

Silvan Scheller *et al.*

*Science* **351**, 703 (2016);
DOI: 10.1126/science.aad7154